Journal of Science: Advanced Materials and Devices 10 (2025) 100965

Contents lists available at ScienceDirect

Journal of Science: Advanced Materials and Devices

journal homepage: www.elsevier.com/locate/jsamd

Research Article

Developing thermally stable strontianite/polymer bio-nanocomposites with enhanced optical and electric properties for optoelectronics and energy storage applications

Turki Alotaibi [a,**], Adel M. El Sayed [b,*]

[a] Department of Physics, College of Science, Jouf University, P.O. Box 2014, Sakaka, Saudi Arabia
[b] Department of Physics, Faculty of Science, Fayoum University, El Fayoum, 63514, Egypt

ARTICLE INFO

Keywords:
$SrCO_3$
Bio-polymer blend
Thermal stability
Band gap tuning
Dielectric relaxation
Energy storage devices

ABSTRACT

Strontianite nanoparticles (STT NPs) were obtained via a facile chemical route and incorporated into chitosan-polyvinyl alcohol (blend) films by the casting technique. STT morphology was studied by TEM. FTIR spectroscopy revealed the physical interaction between the blend's reactive groups and STT NPs. According to XRD results, the STT displayed an orthorhombic structure, and the nanocomposite films exhibited a semicrystalline nature. The films' surface morphology, thickness, and elemental mapping were investigated using SEM and EDX techniques. The thermal analyses showed that the films are thermally stable up to 125 °C, and the main decomposition occurs at 220–375 °C. The films showed transparency in the range of 70–88 %, and the direct/indirect band gaps were decreased to 4.6 and 4.5 eV, respectively, at 2.0 wt% STT content. The DC conductivity of the blend increased from 2.37×10^{-11} to 5.27×10^{-11} S/cm at 2.0 wt% STT content. The nanocomposite films showed enhanced dielectric permittivity and minimal dielectric loss factor in the frequency range of 0.1 Hz–10 MHz. The dielectric and impedance spectroscopies showed that the conduction mechanism is governed by the bulk property of the material, the grain boundary effect, and the STT content. The findings reveal the possible tuning of the optical/electrical properties of the nanocomposite films by STT content to be employed in the optoelectronics and energy storage applications.

1. Introduction

The environmental risks associated with the non-degradable components force the researchers to develop eco-friendly composites using biopolymers [1–4]. The abundance, ease of processing, and safe handling are some advantages of biopolymeric composites [5]. The combination of two biopolymers (biocompatible and biodegradable) is an eco-friendly and green approach that results in the production of a new blend with unique features compared to those of the single polymer [6,7]. Additionally, incorporating 1D/2D materials (fillers) inside the polymer chains is a powerful approach to obtaining novel composites with enhanced mechanical, electrical, optical, thermal, and chemical characteristics [8]. These nano-sized fillers induce interfacial effects, owing to their high surface area and surface energy [9]. Therefore, they can improve and widen the technological applications of the blend to cover optoelectronics, sensors, solar cells, memory devices, and energy storage fields [10].

Bio-nanocomposites based on synthetic polymer polyvinyl alcohol (PVA) and natural polymer chitosan are attracting the attention of various research groups in the biomedical and industrial sectors [11,12]. Chitosan exists in the exoskeletons of some crustaceans, such as crabs and shrimps [13]. It is a biocompatible, biodegradable, linear polysaccharide with NH_2, C–O, and OH (polar) groups found on its surface, allowing it to mix well with both synthetic and natural polymers through dipole-dipole interactions and hydrogen bonding [14]. It is a promising polymer for several medical uses, food packaging, and other applications that require bioactivity, physiological inertness, adhesion, and sorption abilities. However, one of its disadvantages is its tendency to swell and its poor mechanical strength [8,15]. The synthetic PVA exhibits a high dielectric constant, good emulsification and film-forming ability, good viscosity, the ability to absorb electrolytes, and stability in alkaline media [16]. In addition, PVA has promising features such as

* Corresponding author.
** Corresponding author.
E-mail addresses: tbotaibi@ju.edu.sa (T. Alotaibi), ams06@fayoum.edu.eg (A.M. El Sayed).

https://doi.org/10.1016/j.jsamd.2025.100965
Received 14 July 2025; Received in revised form 26 July 2025; Accepted 3 August 2025
Available online 5 August 2025
2468-2179/© 2025 Vietnam National University, Hanoi. Published by Elsevier B.V. This is an open access article under the CC BY-NC-ND license (http://creativecommons.org/licenses/by-nc-nd/4.0/).

biodegradability, flexibility, transparency, toughness, lightweightness, low cost, and non-toxicity, which are needed for several industrial, agricultural, and medical/pharmaceutical applications [17,18]. Its backbone (carbon chain) is adorned with OH groups that tend to form hydrogen bonds. This reactive group enables PVA to form composite films through chemical/physical crosslinking [15]. According to Oreibi et al. [12], Ag/$BaTiO_3$ incorporation can be used to improve the PVA's optical and electric features for optics and quantum applications.

Alharbi et al. [8] studied the impact of CuO/Te_2O_4 on the properties of chitosan-PVA (30:70) blend. Jin et al. [11] found that Ag NPs coated with chitosan-PVA are promising nanocomposites for anticancer treatment for gastric cancer and dyspepsia. Obaid et al. [13] reported that TaC/SiO_2 can be used as a nanofiller to tune the physical properties of PVA-chitosan for γ-ray shielding and photonics devices. Al-Mhyawi et al. [14] developed $FeMoO_4$/polyvinylpyrrolidone (PVP)/chitosan nanocomposites with low dielectric loss and enhanced dielectric constant for electrochemical devices and energy storage applications. Thungphotrakul and Prapainainar [15] investigated the crosslinking effect of citric acid and the addition of chitosan NPs on the antimicrobial activity of PVA/carboxy-methyl-cellulose (CMC) matrices for food packaging applications. Suppanucroa et al. [16] developed MoS_2/chitosan-PVA composite separator with a high conductivity (87.3 mS/cm) and exceptional stability. Faisal et al. [19] fabricated an electrochemical sensor based on Au/ZnO/chitosan for 2-Nitrophenol detection in various environmental materials. Also, Hamza and Habeeb modified the PVA-CMC films with SiO_2/Cr_2O_3 mixed NPs to have suitable features for antimicrobial packaging applications in the food industry [20]. Alizadeh et al. [21] fabricated a drug delivery system based on chitosan-PVA for the adjusted release of some antibiotics. They also used the same blend as an effective antibacterial material for wound dressing. Jose et al. [22] developed Arecanut-residue/chitosan-PVA adsorbent films and achieved 88.68 % removal of 173 mg/L Cr (VI) within 45 min. Blending chitosan with quaternary ammonium-modified PVA increases the separator stability for advanced Zn-air batteries.

On the other hand, strontium compounds have interesting features for the valuable development of thin film-based devices, sensors, solar cells, battery electrodes, supercapacitors, and biomedical applications [23]. One of the most important strontium compounds is strontianite (STT) with an orthorhombic structure at RT and thermal stability up to 1100 °C [24,25]. It is an aragonite-type carbonate found in veins, vugs, limestones, clays, and some ores. It has applications as an industrial material that can be mixed with the ceramic and cement [26]. STT is a bioactive material used by Liu et al. [27] to reinforce the collagen scaffold to enhance the osteoinductivity for bone tissue engineering. According to Hu et al. [28], STT has an indirect band gap of 4.45–4.24 eV, and both ionic and covalent bonding are exist. Nassar et al. [24] prepared STT nanocrystals by the thermal treatment of the oxalate precursor $Sr(C_2O_4)(H_2O)_2$ at 550 °C and then decorated them with Ag for wastewater treatment. Zhang et al. [29] prepared a Co/CoO/STT composite using $Sr(NO_3)_2$ and ethyl glycol/dimethyl foramide (solvent) via a hydrothermal method for efficient electromagnetic wave absorption. Ehsanizadeh et al. [30] reported that adding STT, through the Pechini sol-gel method, reinforced the performance of $SrMnO_3$ for the (electrochemical) hydrogen storage. Moreover, $SrNiO_3$/NiO/STT, prepared by an auto combustion method, worked as an efficient photocatalyst for wastewater treatment through the degradation of organic dyes [31]. Alavi and Morsali [32] reported the formation of STT NPs starting from the Sr acetate and NaOH through a sonochemical method followed by calcination at 400 °C. Gong et al. [33] prepared STT crystals by introducing $SrCl_2$ within a chitosan-gelatin template framework for promoting angiogenesis and bone formation in vivo.

The literature review reveals that chitosan-PVA blend has been used for several applications, including packaging [15], batteries [16], biomedicine [21], and water treatment [22]. Despite vast reports on the preparation and characterization of nanocomposites based on PVA or chitosan in the open literature, as far as could be ascertained, there are no reports on the physical properties of STT/chitosan-PVA nanocomposites. To bridge this knowledge gap, this work aims to synthesize STT NPs as bioactive fillers for chitosan-PVA to obtain bio-nanocomposites for more advanced applications. The STT NPs and nanocomposite films were synthesized using a sol-gel method and casting technique, respectively. These techniques are widely employed as facile techniques for the production of inorganic materials with a proper grain distribution and high-quality polymeric films. Furthermore, the deposition of large-area films and the control of the film's composition and thickness are made easier by solution casting [2,34]. The morphological, structural, thermal, optical, electrical, and dielectric properties of these newly prepared STT/chitosan-PVA nanocomposites were measured, discussed, and compared with those of similar materials. This study's findings suggest that the STT content can control the physical properties of chitosan-PVA, enabling advanced optoelectronic and energy storage applications.

2. Materials and methods

2.1. Materials

Strontium chloride hexahydrate [$SrCl_2{\cdot}6H_2O$, 266.62 g/mol, > 98 %, Merck], oxalic acid [$(COOH)_2{\cdot}6H_2O$, 126.1 g/mol, 99 %, Adwik, Egypt], and double-distilled water were used for $SrCO_3$ (STT NPs) preparation. PVA [Avondale Lab., Banbury-Oxon, UK, 17,000 g/mol] and chitosan [more than 70 % deacetylated, 110,000 g/mol, DOP Organic Kimya, Turkey] were used for films preparation.

2.2. Preparation

Solution 0.8 M was prepared by dissolving 21.33 g of $SrCl_2{\cdot}6H_2O$ in 100 mL of water by stirring using a bar magnet and heating at 55 °C. After the complete dissolving, about 10.1 g of $(COOH)_2{\cdot}2H_2O$ was added under stirring that continued for 2 h. The final solution was aged for one day and got rid of excess of water by evaporation at 110 °C. The obtained gel was calcined at 450 °C/2 h in a ceramic oven to form STT powder, according to the equation:

$$SrCl_2 \cdot 6H_2O + (COOH)_2 \cdot 2H_2O \xrightarrow{\Delta(450^\circ C)/2h} 2SrCO_3 + 2H_2O \uparrow + 4HCl \uparrow \quad (1)$$

0.7 g of PVA/50 mL water was dissolved by stirring at 85 °C/2 h (solution A). 0.3 g of chitosan was dissolved (at room temperature (RT) ~28 °C) in 50 mL water/2 % acetic acid by stirring for 1 h (solution B). The blend solution was prepared by mixing the solutions A and B by stirring for 1 h at RT. The chitosan-PVA ratio (30 %/70 %) yields a solution of suitable viscosity for good dispersion of STT. The composite films were obtained by adding 1.0, 2.0, and 4.0 wt% of STT, which were calculated using the equation [10,34]:

$$x\ (\mathrm{wt\%}) = \frac{W_{STT}}{W_{STT} + 1} \times 100 \quad (2)$$

where W_{STT} is the required mass of STT, and "1" is the total mass of PVA and chitosan. The determined W_{STT} was dispersed in 20 mL of water by ultrasonication for 10 min before mixing with the blend solution. The composite solutions were stirred for an additional 2 h at RT to ensure a homogenous distribution of the STT. The blend and composite solutions were put in Petri dishes for 5 days to evaporate at RT and then heat-treated at 40–50 for 2 h to get self-standing films for characterization and measurement.

2.3. Characterization techniques and measurements

High-resolution (HR) TEM (JEM 2100-JEOL) was operated at a voltage of 200 kV to investigate the morphology of chemically prepared STT. The vibrations of the chemical/functional groups in STT, chitosan-

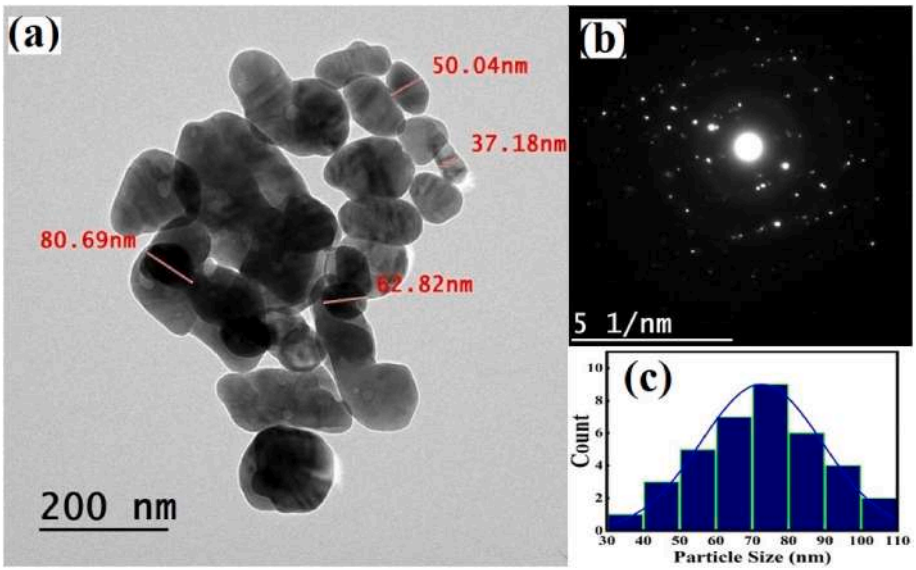

Fig. 1. TEM investigation of STT NPs: (a) shape and size, (b) SAED of a single particle, (c) histogram of particle size distribution.

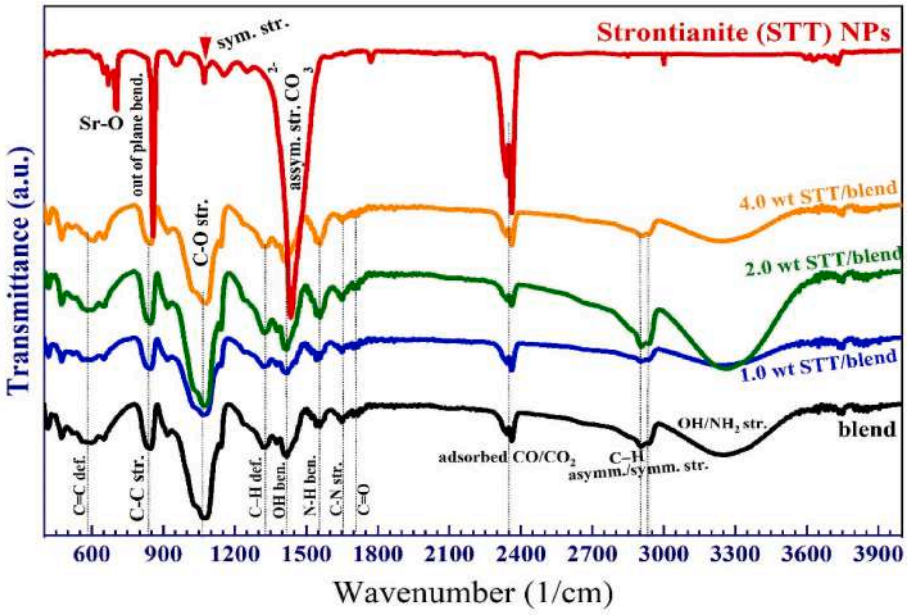

Fig. 2. Transmittance (FTIR) spectra of STT NPs and its impac on the vibration modes of chitosan-PVA blend.

PVA and composites were investigated in the 4000–400 cm^{-1} wavenumber range using the attenuated-total-reflectance (ATR) Fourier-transform infrared spectrometer supplied by Bruker-Vertex/70. The XRD patterns and data for the fillers and films were obtained by using a diffractometer supplied by RIGAKU, Smart-Lab. The equipment provides K_α emission of wavelength $\lambda = 1.544$ Å, and the measurement is carried out in the 2 θ range of 10–80° with an interval of 0.02°. The film's morphology, cross-section, and film thickness were checked and determined by a SEM (scan-electron-microscope), Inspect/S/FEI, Holland. The chemical composition (existing elements) and distribution (elemental mapping) were investigated by FE-SEM, QUANTA/200F, SE-BSE-EDX. The thermal stability and transition temperatures were studied using a Perkin-Elmer-STA-6000, in the 28–600 °C temperature range and under the flow of N_2 gas. The optical transmittance/absorption were recorded in the 200–1400 nm wavelength by a Shimadzu UV-3600 spectrophotometer (UV/Vis/NIR). The dielectric parameters (permittivity, loss, conductivity, modulus, and impedance) were studied with the help of Novocontrol turnkey 40 broad-band dielectric spectroscopies in the 0.1 Hz–10 MHz at RT.

3. Results and discussion

3.1. The structure and morphology of filler and films

3.1.1. HR-TEM investigation

The TEM device provides valuable insights into the nanomaterials' shape (morphology), crystallinity, and size. Fig. 1(a) shows that the chemically prepared STT takes on nanoparticle (NPs)-like morphology. Some particles tend to agglomerate due to the nanosized materials' high surface area and surface energy. Fig. 1(b) is the special (selected) area electron diffraction (SAED) for a single particle. The white spots and rings indicate the polycrystalline nature of the material. Fig. 1(c) is the histogram of particle-size distribution, deduced from Fig. 1(a) utilizing the ImageJ software. The sizes of these NPs are in the range of 30–110

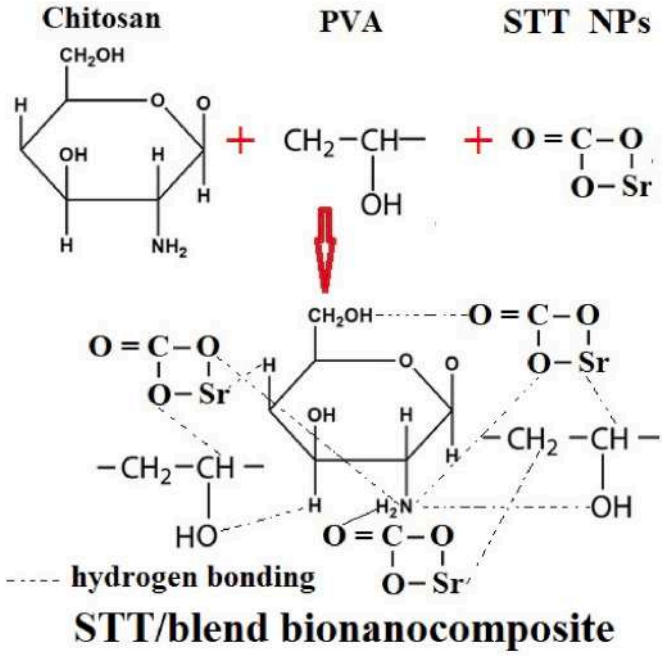

Scheme 1. Illustration for the possible interactions in STT/chitosan-PVA nanocomposite.

nm, with an average size of 70 nm. A similar result was reported by Alavi and Morsali [32]. Gong et al. [33] reported the formation of STT within a chitosan-gelatine template, with a fan-like morphology and closed spheres.

3.1.2. ATR-FTIR spectroscopy

Fig. 2 displays the FTIR spectrum of STT NPs, chitosan-PVA blend, and STT/blend nanocomposite films. The bands attributed to the vibrations in carbonate (CO_3^{2-}) anions in the STT are seen in the 400–1800 cm^{-1} region [32]. The sharp and intense band at 2350 cm^{-1} arises from CO/CO_2 adsorbed from the surroundings [35]. The wide and strong band around 1446 cm^{-1} and the relatively small band at 1070 cm^{-1} are assigned to the stretching vibration asymmetric/symmetric modes of CO_3^{2-} ions [24,31]. In addition, the narrow and sharp band at 860 cm^{-1} is attributed to the CO_3^{2-} bending (out-of-plane) vibrations [31]. The two bands at 670 and 698 cm^{-1} are assigned to the vibrations of Sr–O bonds [17].

The spectrum of the blend shows a broad band in the range of 3000–3550 cm^{-1} that is owed to the combined vibration of OH/NH_2 in stretching mode [8,35]. The C–H alkyl asymmetric/symmetric stretching (two adjacent) bands are found at 2937 and 2898 cm^{-1}. The intensity of these peaks is sensitive to STT content due to the hydrogen bond formation and the electrostatic interaction between Sr^{2+}/ HO^- and CO_3^{2-}/ NH_3^+ (protonated NH_3 because of the presence of acetic acid). The bands at 1716, 1652 cm^{-1} and 1558 cm^{-1} arise from the C═O (amide group) stretching, C–N stretching, and N–H (in NH_3^+ or the ionized primary amino groups) bending, respectively [19,21]. The OH bending and C–C stretching/–CH_2 rocking are visible at 1417 and 846 cm^{-1}, respectively [21,22]. The wide and strong band extending from 950 to 1150 cm^{-1}, and centered at 1080 cm^{-1} belongs to the C–O stretching [14]. The band at 1326 cm^{-1} refers to the in-plane C–H deformation, and that at 580 cm^{-1} to the stretching modes of C═C [8].

The spectra of 1.0–4.0 wt% STT/blend composites are similar to pure blend, where no new bonds are formed. This indicates no chemical interactions in the nanocomposite films. However, the changes in the peaks' intensity and width of most of the peaks, as well as the change in some peaks' positions (the C═C band shifted from 580 to 609 cm^{-1} with

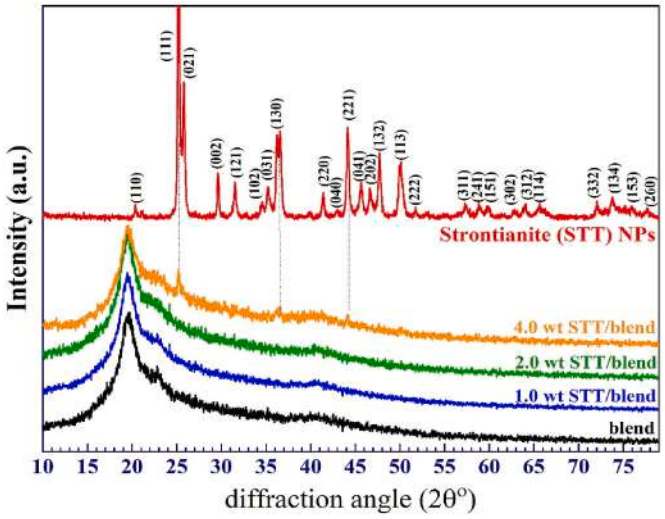

Fig. 3. XRD pattern of STT NPs and its impac on the structure of chitosan-PVA blend.

the increment of the filler content to 4.0 wt%), indicate the electrostatic interaction and inter-intramolecular hydrogen bonding among the matrix's constituents [11,16]. These interactions are illustrated in Scheme 1. This physical interaction and complexation are owing to the reactivity and uniform distribution of the fillers throughout the composite films, which in turn should alter the physical properties of the films. Therefore, more characterizations are required before investigating the optical, thermal, and dielectric features of the prepared materials.

3.1.3. XRD patterns

Fig. 3 shows XRD charts of STT, blend, and nanocomposite films. The XRD chart of STT indicates the polycrystalline nature. The positions (and Miller's indices) of the main peaks are at 2θ = 25.18° (111), 25.79° (021), 29.58° (002), 31.27° (121), 35.25° (031), 36.53° (130), 41.38° (220), @ 44.13° (221), 47.69° (132), and 49.89° (113). The observed peaks at these positions and with these intensities match well with the data of strontianite of orthorhombic structure, lattice parameters: a = 5.098 Å, b = 8.4166 Å, c = 6.0337 Å, $\alpha = \beta = \gamma = 90°$, space group 62: *Pmcn*, and DB card number 9013802. Similar findings were reported for STT nanocrystals prepared by the thermal annealing of oxalate salt [24], the hydrothermal method [29], the Pechini sol-gel [30], and a sonochemical technique [32]. The average crystallite size (determined considering the Scherrer equation) was found to be 32.7 ± 2.5 nm. The sizes determined by XRD and TEM (Fig. 1(a)) differ due to the nature of these techniques. The first is an indirect technique that gives the crystallite size, whereas the second is a direct technique that gives the particle (grain) size. Each grain consists of one or more crystallites. Similar results were found for nanosized La/Na-doped ZnO films [36].

The wide and intense peak in the blend's XRD pattern located around 2θ = 19.44° and the less intense one at 2θ = 41.2° confirm the presence of PVA with a semicrystalline structure [37]. In addition, the peak at 2θ = 23° refers to the presence of chitosan (amorphous structure) [14,38]. In a previous study, another two peaks were detected in the chitosan pattern (due to its hydrated-crystalline structure) at 2θ = 11.6° and 18.5° [35]. However, it seems that these peaks are submerged inside the amorphous regions of PVA (the major component of the blend, *i.e.,* 70 %). Interestingly, the widths and intensity of the principle XRD peaks of the blend decreased with increasing STT content beyond 1.0 wt%, indicating the decrease in the crystallinity degree of the films. A similar finding was reported for PVA loaded with 2–6 wt% SrO NP [17]. This suggests the hydrogen bonding and interaction between the filler and polymeric matrix and indicates the dominance of STT functional groups

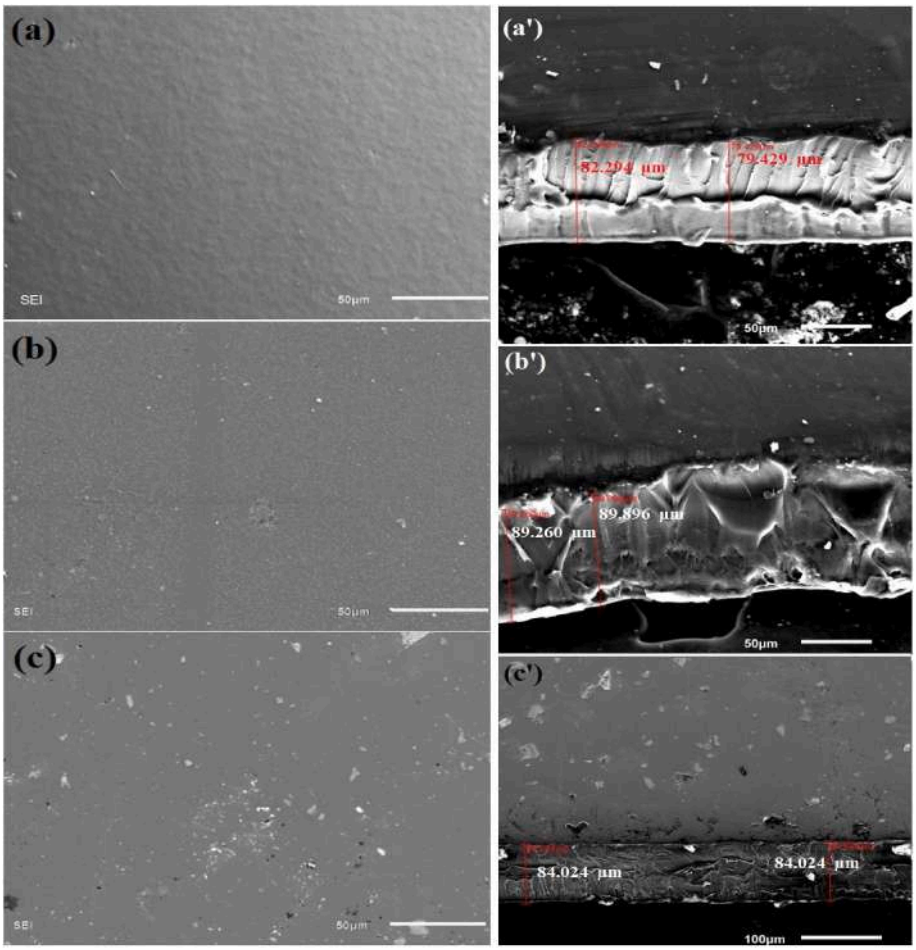

Fig. 4. (a–c) top-view SEM images for the blend film and the films doped with 2.0 and 4.0 wt% STT NPs. (a'–c') are the cross-sectional view of the three films.

[30]. These results are consistent with FTIR results. At 4.0 wt% STT content, the most intense peaks (planes) in the XRD pattern of STT; (111) @ 25.18°, (130) @ 36.53°, and (221) @ 44.13° are seen superimposed on the blend pattern, without any shift in the peak position. This detection may be due to some agglomeration that occurred because of the high energy at the surface of the fillers and their tendency to aggregate when they come closer together. Also, this result indicates that the blend can't alter the crystal structure of the STT. A similar note was reported for STT/chitosan (70 %)-gelatin (30 %) composite, where the two peaks (021) and (111) of STT were found to merge into a broad peak [33].

3.1.4. Morphology and chemical analysis investigation

The film morphology and filler distribution on the films' surface are shown in Fig. 4(a–c), where the films have a homogenous surface, indicating the compatibility between chitosan and PVA, without forming pores or cracks. The filler content of 2.0 wt% is uniformly distributed, but when the ratio increased to 4.0 wt% some agglomerations for STT were seen. The aggregation of nanofillers in the polymer matrix is a natural phenomenon, where the high surface energy forces them to agglomerate when the particles get close together [17].

The incorporated fillers didn't alter the surface structure of the films. Fig. 4(a'–c') shows the cross-section of the blend, 2.0 wt% and 4.0 wt% STT-loaded blend films. These images confirm the compatibility between chitosan and PVA and confirm the presence of STT fillers inside the film's surface. The thicknesses of the blend and 2.0 wt% STT and 4.0 wt% STT, are about 80.86 µm, 89.58 µm, and 84.02 µm, respectively. The relatively higher thickness at 2.0 wt% STT could be owing to the formed pores at the lower edge of the film.

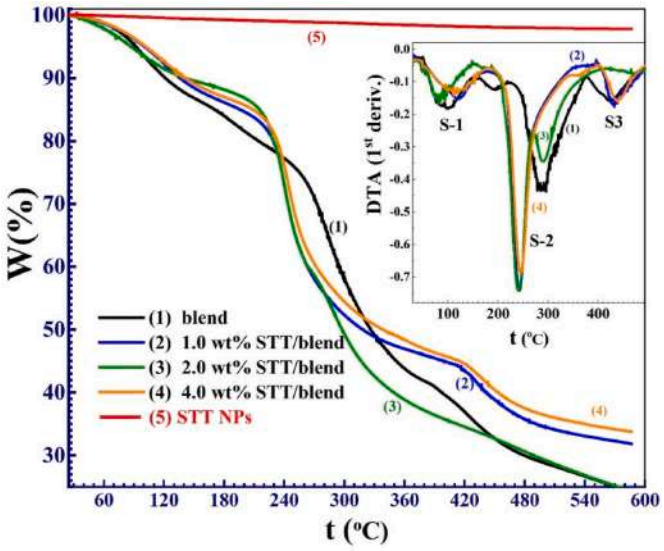

Fig. 5. TGA thermograms of STT NPs, blend and STT/blend nanocomposites.

The chemical composition of the chitosan-PVA blend and the film loaded with 4.0 wt% STT NPs are shown in Fig. S1(a and b). The blend and nanocomposite film are mainly composed of H (not seen in the EDX spectra), C, O, and N (of chitosan). These elements appear as single peaks at about 0.28 keV (C K_α) and 0.52 keV (C K_α), and in between, N K_α

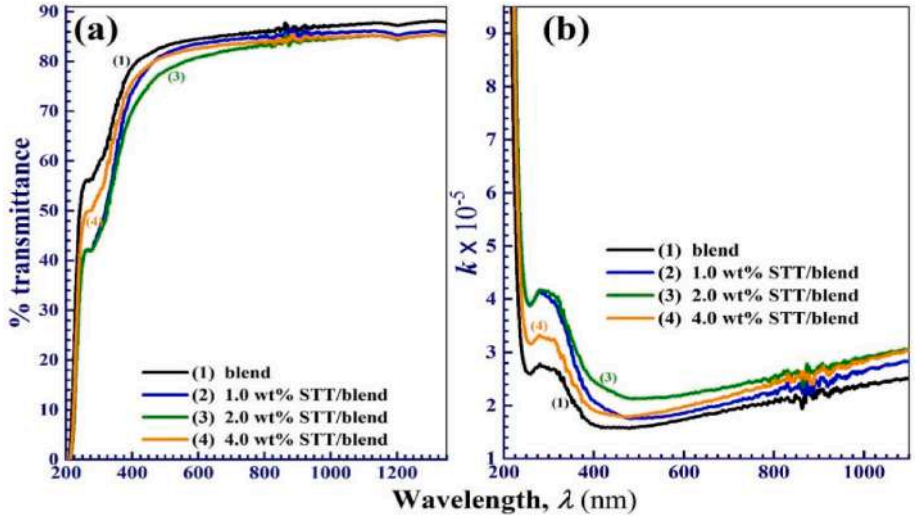

Fig. 6. The impact of STT NPs (1.0–4.0 wt%) on (a) the transmission and (b) *k* index of chitosan-PVA.

exists at 0.4 keV. The [C]/[O] atomic ratio is 30.54/67.07. The small content of [N] is attributed to the low content (30 %) of chitosan in the blend. Fig. S1(b) shows that Sr exists at 1.8 keV (main peak, L_α) and 1.88 keV (shoulder, L_β). The recorded wt% value of Sr (inset table) is 3.03 %, which is close to the added ratio (4.0 wt%) during the preparation process. Loading STT NPs changed the chemical composition of the blend, causing the [C]/[O] atomic ratio to become 31/66.78 and [N] to decrease from 2.4 to 1.7 at%. These results confirm the presence of Sr atoms in the nanocomposite films. The elemental mapping and the uniform distribution of the elements in the 4.0 wt% STT/blend film are shown in Fig. S2 (see the supporting information).

3.2. Thermal stability

Thermal stability is a key feature of the composite films and can be studied through thermogravimetric analysis (TGA). Fig. 5 shows the relation between the weight loss (W%) and the applied temperature. STT shows excellent thermal stability till 600, where the W% is about 13 %. This loss arises because of the removal of moisture and CO_2 adsorbed from the surroundings and appears in the FTIR spectrum of STT, Fig. 2. Chen et al. [25] reported that the co-precipitated STT NPs, 40–80 nm in size, is thermally stable and begin to convert to SrO at a temperature ≥1100 °C.

The inset of this figure is the differential thermal analysis (DTA, *i.e.,* the 1st derivative of the weight loss relative to the temperature). This derivative shows the stages of W% and the main decomposition. An initial weight loss (W_o%) of about 8–10 % is observed for the composite films with increasing the temperature from RT to 125 °C. This is the first stage (S-1 in the inset) of W%. For the blend, this range is reduced to RT–118 °C, which is the first indication of the enhanced thermal stability after loading STT NPs. This W_o% loss is attributed to the moisture evaporation and adsorbed CO_2, seen at 2350 cm^{-1} in the FTIR spectra. In the temperature range of 135–220 °C, the composite films lose only 13 % of their initial weight (a negligible W%), while the pure film loses 17 %. This finding indicates that the composite films are more thermally stable, and this enhancement can widen the blend's applications for various practical utilizations, such as space applications, electrochemical devices, the packaging industry, and environmentally friendly uses, to a temperature of 220 °C.

The main decomposition (maximum weight loss rate) for the composite films (S-2 in the inset) occurs in the temperature range 220–375 °C and indicates the chain degradation and cleavage of the chitosan polymer backbone. At the centre of this stage, the maximum thermal degradation temperature is 290 °C for the pure blend and 243 °C for the 4.0 wt% STT/blend composite, as seen in the inset of the figure. The 3rd stage (S-3) occurs at a temperature > 380 °C. In this stage, PVA decomposition and degradation/carbonization of smaller chains occur [39]. At temperatures of > 480 °C, the remaining W% is of the residual char. The 4.0 wt% STT/blend retains a W% of about 35 %, compared to the pure matrix (25 %). This significant difference indicates that the nanocomposites exhibit enhanced thermal stability [8]. For more information about the transition temperatures of the samples, Fig. S3 depicts the DSC (differential scanning calorimetry) thermograms of the STT NPs and polymeric films. The STT NPs curve does not indicate any transitions. The blend and nanocomposite films display about three or four endothermic peaks. The glass transition temperatures are not observed for all films.

Table 1
Transmittance (T%), band gaps and index of refraction of films.

Film	T% (600 nm)	Band gaps (eV)		n_1	n_2	$\bar{n}$
		E_{gi}	E_{gd}			
Blend	84.56	4.9	5.2	1.97	2.38	2.17
1.0 wt% STT NPs	83.54	4.6	4.8	2.03	2.43	2.23
2.0 wt% STT NPs	80.84	4.5	4.6	2.06	2.46	2.26
4.0 wt% STT NPs	82.67	4.7	5.0	2.00	2.40	2.20

3.3. Optical study

Investigating the optical spectra of the polymeric materials and determining the key optical parameters are essential for optoelectronic devices and practical uses. Fig. 6(a) shows the impact of STT NPs on the transmission (T%) of the chitosan-PVA blend. All films exhibit a sharp increase in T% with λ in the UV region and T% in the range of 70–88 % in the visible-IR spectrum. This high T% with the thermal stability of the films, discussed in the previous section, encourages the employing of these materials in practical utilizations such as coatings and food packaging [40]. At $\lambda = 600$ nm, the blend exhibits 84.5 % transmittance and decreases to 80.8 % at 2.0 wt% STT NPs content because of the uniform distribution of the fillers, which scatter and absorb a portion of the incident light. A similar finding was reported for the blend modified with 2.0 wt% SiO_2/TaC [13]. T% slightly increased to 82.7 % at 4.0 wt% STT. These values are listed in Table 1. This is related to the structural changes in the composite film, such as thickness and the agglomerations of STT, seen in Fig. 4(c, c').

The absorption index (*k*) is determined from the absorption (Abs) spectrum of the film using the equation [41]:

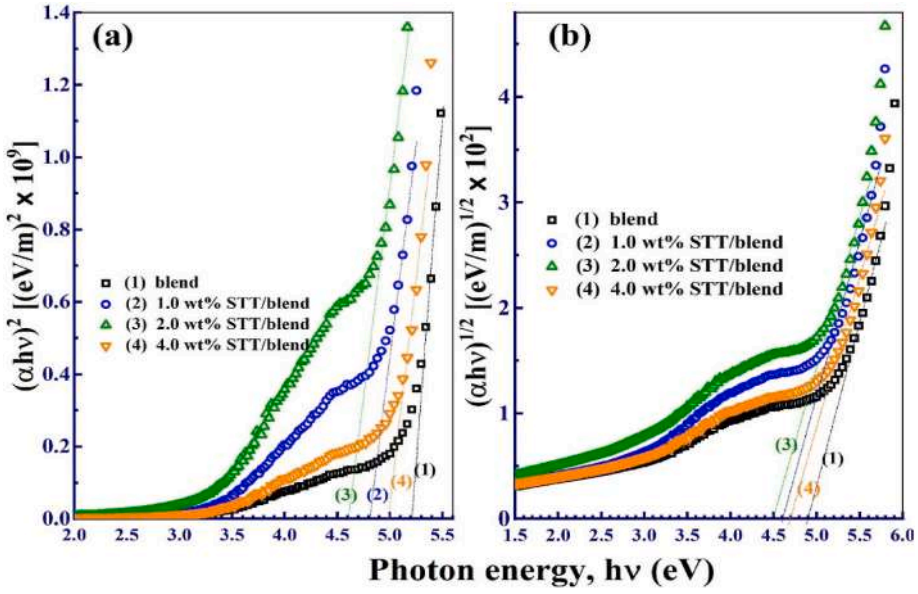

Fig. 7. The impact of STT NPs (1.0–4.0 wt%) on (a) the direct (E_{gd}) and (b) indirect (E_{gi}) band gaps of chitosan-PVA blend.

$$k = \frac{\lambda.\mathrm{Abs}}{4\pi d} \tag{3}$$

where d is the thickness of the films. Fig. 6(b) displays the k variation with λ, where the films have $k < 10^{-4}$ and increase with STT NPs content till 2.0 wt% and decrease at 4.0 wt% STT NPs. The k spectra exhibit a broad band extending from 255 to 350 nm, arising because the absorption takes place by the unsaturated bonds ($\pi \rightarrow \pi^*$ electronic transition). The absence of any absorption bands under the influence of visible (380–780 nm) photons confirms the high transparency of the nanocomposites [8]. At $\lambda \geq 500$ nm, the values of k rise linearly with λ, and this result could be exploited for the development of optoelectronic and sensor devices.

Accounting for the possible electronic transitions, band gap (E_g) structure, and the index of refraction (n) is a necessity for device fabrication. Applying Tauc's equation [10]:

$$(h\upsilon\alpha)^{1/r} = C(h\upsilon - E_g) \tag{4}$$

where the light (photon) energy $h\upsilon = \frac{1.242\ \mathrm{keV}}{\lambda\ (\mathrm{nm})}$, $\alpha = \frac{2.303 \times \mathrm{Abs}}{\text{film thickness}}$ is the absorption coefficient, C is the band tailing constant, and $r = ½$ and 1 for the direct (E_{gd}) and indirect (E_{gi}) band gaps, respectively. Fig. 7(a, b) depicts Tauc's plots for the possible direct [$(\alpha h\upsilon)^2$ vs. $h\upsilon$ plots] and indirect [$(\alpha h\upsilon)^{0.5}$ vs. $h\upsilon$ plots] transitions. According to Tauc's theory, extending the straight-line regions on the $(\alpha h\upsilon)^2$ vs. $h\upsilon$ and $(\alpha h\upsilon)^{0.5}$ vs. $h\upsilon$ to $\alpha = 0$ gives E_{gd} and indirect E_{gi}, respectively. The E_{gd} and E_{gi} of chitosan-PVA are 5.2 and 4.9 eV, respectively, reduced to 4.6 and 4.5 eV with STT NPs content of 2.0 wt%. Then, they increased to 5.0 and 4.7 eV, respectively, at the 4.0 wt% STT NPs ratio. The variation of E_{gd} and E_{gi} with STT content is summarized in Table 1.

Similarly, 2.0 wt% SrO NP narrowed the PVA's E_{gd} from 5.1 to 3.9 eV, and increasing the filler's content to 6.0 wt% decreased the E_{gd} to 3.7 eV only [17]. A study conducted by Algethami [42] reported that the E_{gd} and E_{gi} of chitosan-PVA (70 %:30 %) blend decreased from 5.4 to 5.01 eV to 4.46 and 3.49 eV, respectively, after the incorporation of 5 % GO/5 %TiO_2. 1.0 wt% $NaTiO_3$ reduced the E_{gd} and E_{gi} of the chitosan-PVA (50 %:50 %) from 5.2 to 4.4 eV to 4.9 and 4.0 eV, respectively [39]. According to Obaid et al. [13], 6.6 wt% SiO_2/TaC mixed nanofiller has reduced the E_{gi} of the chitosan-PVA from 4.7 to 3.3 eV. Additionally, the E_{gd}/E_{gi} of pure chitosan-PVP decreased from 4.5/4.0 eV to 3.5/2.9 eV at 2.6 wt% $FeMoO_4$ content [14]. These results

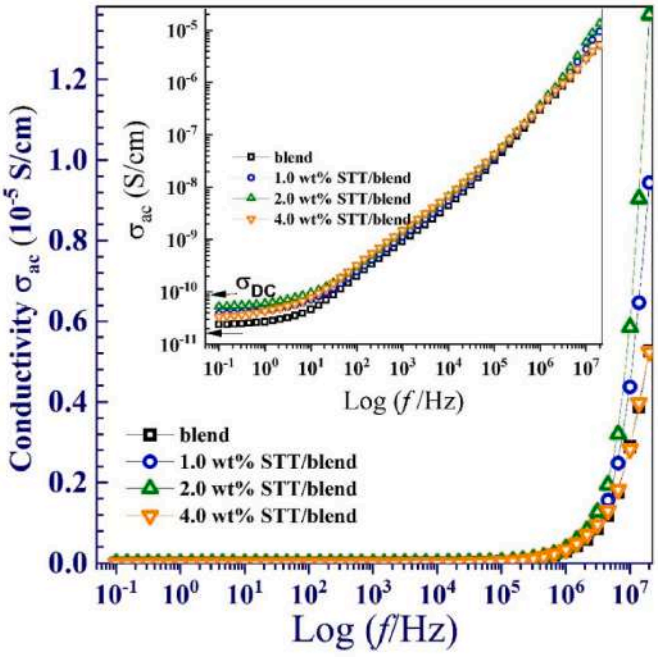

Fig. 8. The ac conductivity of the chitosan-PVA loaded with 1.0–4.0 wt% STT NPs. The inset is used to get σ_{DC} values (σ_{ac} at $f \rightarrow 0$).

indicate that *i*) both direct and indirect transitions are allowed in the prepared materials, and E_{gd} and E_{gi} can be tuned by STT NPs content. *ii*) low contents (1.0 and 2.0 wt%) of STT NPs with uniform distribution, as seen in SEM images (Fig. 4), induce defects and sub-energy levels inside the band gap, which improves the semiconducting behaviour of the films.

There are various models to determine the n values from E_{gd} values. Two of the most common equations are [43,44]:

$$\frac{n^2-1}{n^2+2} = 1 - \sqrt{\frac{E_{g.d}}{20}} \text{ and } n = \sqrt{\frac{12.417}{\sqrt{E_{g.d} - 0.365}}} \tag{5}$$

The values of n were calculated using the two models, and the obtained values n_1 and n_2 and their average values ($\overline{n}$) are put in Table 1.

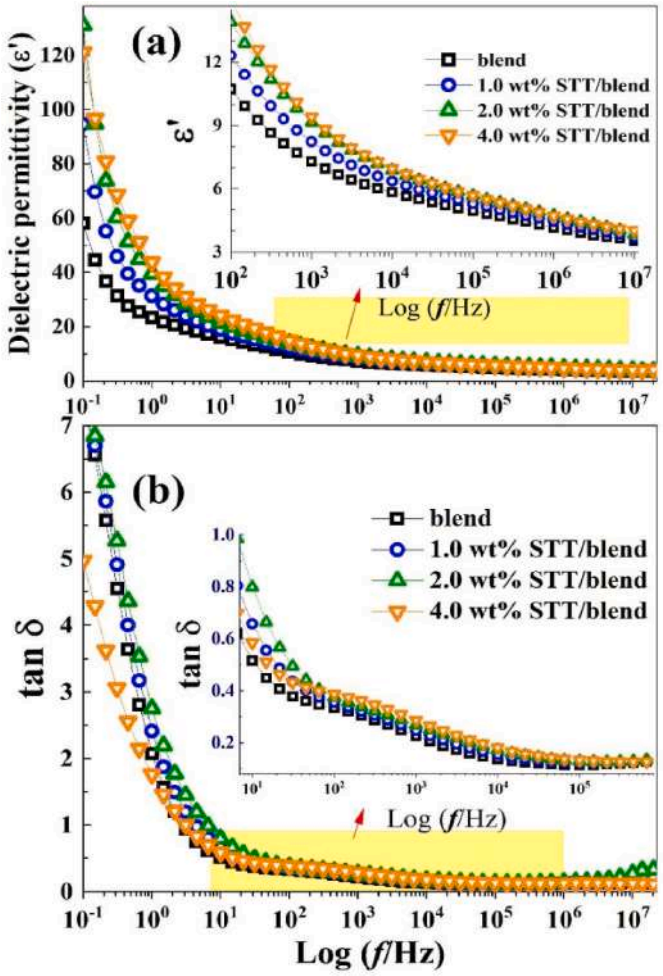

Fig. 9. (a) real dielectric permitivity and (b) loss tangent of the STT/blend films.

The obtained *n* values for the blend are consistent with a previous study [39]. The $\bar{n}$ values increased from 2.17 to 2.26 at 2.0 wt% STT NPs. The uniform distribution of the STT NPs enables the filler to act as scattering centres and increase the film's reflectivity. At 4.0 wt% STT NPs ratio, the $\bar{n}$ decreased to 2.2, *i.e.*, they are inversely proportional with E_{gd}. These results confirm the facile tuning of the optical features of the blend by STT NPs content.

3.4. Dielectric spectroscopy

3.4.1. AC and DC conductivity

Fig. 8 shows the variation of the AC conductivity (σ_{ac}) with the applied *f* ranging from 0.1 Hz to 10 MHz. The inset of the figure shows Log σ_{ac} vs. Log (*f*). At low *f*, the curves are flattened (*f*-independent), which means that the conductivity is assigned to the DC conductivity. The chitosan-PVA blend shows $\sigma_{DC} = 2.37 \times 10^{-11}$ S/cm, increased to 5.27×10^{-11} S/cm at 2.0 wt% STT NPs due to the filler's semiconducting nature and uniform distribution, and then decreased to 3.35×10^{-11} S/cm at 4.0 wt% content due to the filler agglomeration and the induced structural changes at this ratio. At $f = 1 \times 10^{1}$–5×10^{6} Hz, the σ_{ac} predominates and increases almost linearly with *f*. At high *f*, the observed frequency-dispersion indicates that the charge carriers gain enough energy to overcome the barrier, and the uniformly distributed STT NPs may form a 3D connected network that facilitates the charge carrier movement [18,45].

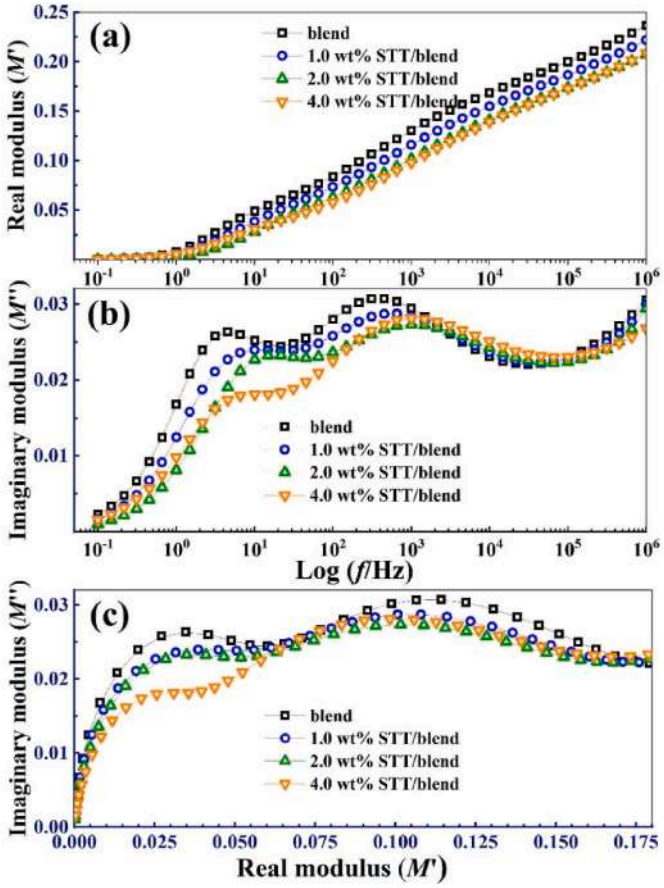

Fig. 10. (a) the real, (b) imaginary electric modulus, and (c) Cole-Cole (Argand) plots for the blend loaded with 0–4.0 wt% STT NPs.

3.4.2. Permittivity and electric modulus

The complex dielectric permittivity (ε^*) and complex electric modulus (M^*) are related by the following equations [2,46]:

$$\varepsilon^* = \varepsilon' - j\varepsilon'' = \frac{1}{M^*} \tag{6}$$

$$M^* = M' + jM'' = \frac{\varepsilon'}{\varepsilon'^2 + \varepsilon''^2} + j\frac{\varepsilon''}{\varepsilon'^2 + \varepsilon''^2} \tag{7}$$

where ε' (ε'') is the real (imaginary) part of dielectric permittivity, and M' (M'') is the real (imaginary) electric modulus. Fig. 9(a) shows the $\varepsilon'(f)$ of the blend before and after loading with 1.0–4.0 wt% STT NPs. There is a strong frequency (*f*) dispersion for all films at low *f*, and a close *f*-independent behaviour at higher *f* ($f \geq 10^4$ Hz), as seen in the inset of the figure. The molecules of the blend can change their orientation following the applied electric field direction in the low-*f* side, causing the observed increase in the ε' values [1,47]. As *f* increases, the molecules and dipoles become unable to (can't) follow the ultra-high change in the electric field direction, and therefore the charge carrier's concentration at the grain boundary decreases, causing the observed decrement in ε'. STT NPs with the uniform distribution on the surface and inside the blend induce some heterogeneity and create/increase the interfacial polarization. Hence, the ε' values increased with STT content.

Fig. 9(b) shows the dielectric loss factor tan δ, where tan $\delta = \frac{\varepsilon''}{\varepsilon'}$. The films exhibit high tan δ values at small *f*. This indicates the grain boundary dominance in the low *f*-side, where the segmental motion and charge carriers require high energy to jump from one place to another. With increasing the applied *f*, the resistive effect of the grain boundaries becomes dominant, and therefore the required energy for segmental/carrier motion becomes marginal. At high *f*, the orientation polarization

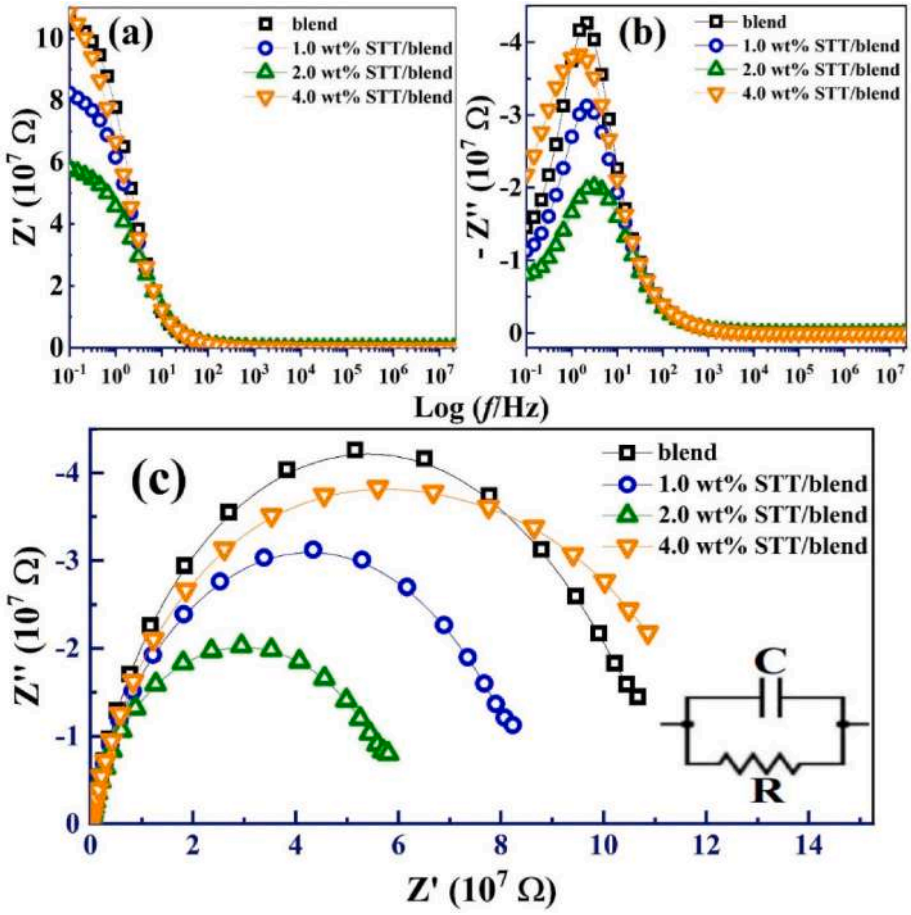

Fig. 11. (a) real, (b) imaginary impedance and (c) Z'-Z'' (Nyquist) diagrams for the blend loaded with 0–4.0 wt% STT NPs. The inset of (c) represents the equivalent circuit.

needs more time than the electronic and ionic polarizations. Hence, only the last two types of polarizations play an essential role, resulting in the observed decrease in tan δ. Two important notes should be mentioned here: *i*) the blend and 1–2 wt% STT-loaded films display almost the same values of tan δ, but the 4.0 wt% STT/blend has the lowest values of tan δ at $f \leq 10$ Hz. Similar results were reported for chitosan-PVP loaded with $FeMoO_4$ NPs, where increasing the filler content to 3.6 wt% caused particle agglomeration and decreased the interfacial interaction per unit volume [14]. *ii*) at $f > 10$ Hz, all films have very low tan δ (< 0.8), as seen in the inset of this figure. *iii*) The enhanced ε' and the minimal tan δ make these nanocomposites function as energy-harvesting equipment. A high ε' enables efficient storage for the electrical energy in energy storage devices/capacitors. The minimal tan δ ensures the lowest energy dissipation, which makes the material suitable for high-f circuits and telecommunications [3].

The electrical energy a material can store in the unit volume is proportional to its dielectric permittivity and the square of the applied electric field E, *i.e.*, $E_d = \frac{1}{2}\varepsilon_o\varepsilon' E^2$ [7,34]. Fig. S4 shows the calculated E_d for the blend and STT/blend films, where E_d is in the range of (0.2–8) x 10^{-3} J/m^3. These values are smaller than those reported in Ref. [10] for Cr_2O_3/PVA/CMC. At low f, E_d is increased with the STT NPs ratio. However, at higher f (10^4–6×10^6) Hz, E_d is not impacted by increasing STT NPs content from 2.0 to 4.0 wt%.

According to equation (6), the M^* is as the reciprocal ε^*. Compared to ε^* formalism, M^* exhibits a greater advantage towards the relaxation mechanism due to the depolarization effects that dominate ε^* formalism is suppressed [2,47]. Fig. 10(a, b) shows the spectra of both M' and M''. At low f, the M' tend to zero value, indicating the suppression of the electro-depolarization effects (negligible) in the low-f side. M' values increase linearly with f, and decrease slightly with increasing STT NPs content. This indicates that the uniform distribution of STT NPs inside the blend encourages the short-range mobility of the charge carriers. In the M'' spectra, all films exhibit two asymmetric relaxation peaks, with a shift to higher f upon loading STT NPs. The first one is related to the bulk property of the films, and the second semi-circles indicate the contribution of the grain boundary to the conduction mechanism [2,18,48]. The two sides of each relaxation peak represent the tuning of the charge carrier mobility from a long range to a shorter one.

3.4.3. *Impedance and nyquist diagrams*

The measured real (Z') and imaginary (Z'') parts of the impedance are shown in Fig. 11(a and b). Z' provides information about the resistive part, and Z'' represents the reactance originated from the capacitive/inductive nature of the blend system [1,6]. The peak height of Z'' decreases with increasing STT NPs content till 2.0 wt%, which indicates the decrease of grain boundary resistance due to the created conductive network or pathways for charge carrier motion inside the matrix [3,6,18]. At the intermediate and higher f (> 100 Hz), the values of Z' and Z'' of the films are merged (become comparable) due to the space charge accumulation, the release of spatial charges in the films, and the limited interfacial polarization [49,50]. Figs. 8 and 11(a) show that σ_{ac} and Z' are inversely proportional to each other. The charge carriers can tunnel through the proposed 3D conductive channels/pathways through the uniform distribution of the filler, resulting in the observed decrement in Z'. Fig. 11(c) shows that the Z'-Z'' (Nyquist plots), where the arcs are centered below the Z'-axis, which means that the conduction mechanism in these composites commits to the Cole-Cole model, not the Debye one

[3]. These semicircles can be represented by a bulk capacitance (C)//bulk resistance (R), as shown in the inset of Fig. 11(c). The (C) is due to the immobile blend chains, and the (R) concerns the charge carrier's migration [5]. The decrease of the radii of these semi-circles with STT NPs content till 2.0 wt% confirms the enhancement of the semiconductor characteristics of the materials [3,46,47], as revealed by decreasing E_g values.

4. Conclusion

Facile chemical routes were employed for the preparation of orthorhombic STT NPs (33 nm in size) and STT/chitosan-PVA semicrystalline films. The FTIR spectroscopy revealed the physical interaction and hydrogen bonding between the blend chain and STT NPs. TEM, XRD, and SEM analyses revealed the polycrystallinity and tendency of STT NPs to agglomerate at a content >2.0 wt%. TGA thermograms showed that STT NPs are thermally stable up to 125 °C and decompose mainly at 220–375 °C. The films showed transmission of 70–88 % and a low absorption index ($k < 10^{-4}$). The direct and indirect E_g decreased from 5.2 to 4.9 eV to 4.6 and 4.5 eV, respectively, at 2.0 wt% STT NPs content. In addition, the index of refraction increased from 2.17 to 2.26 and then decreased to 2.2 at 4.0 wt% STT NPs content. Loading 2.0 wt% STT NPs increased the blend's σ_{dc} from 2.37×10^{-11} to 5.27×10^{-11} S/cm. STT/chitosan-PVA showed enhanced dielectric permittivity and minimal dielectric loss at $f > 10$ Hz. The electric modulus and impedance spectroscopy showed significant dependence of the STT-added ratio and the applied f. Two relaxation peaks are observed owing to the bulk properties and grain boundary contributions in the conduction mechanism. The Nyquist plots showed a significant decrease in the impedance at 2.0 wt% STT NPs. In summary, STT NPs incorporation has enhanced the thermal stability with the tunable optical and electric properties, which can be employed for optoelectronics and energy storage.

CRediT authorship contribution statement

Turki Alotaibi: Writing – original draft, Validation, Methodology, Investigation, Funding acquisition, Formal analysis, Conceptualization. **Adel M. El Sayed:** Writing – review & editing, Writing – original draft, Visualization, Software, Resources, Methodology, Investigation, Formal analysis, Data curation, Conceptualization.

Data availability

No data was used for the research described in the article.

Declaration of interests

The authors declare that they have no known competing financial interests or personal relationships that could have appeared to influence the work reported in this paper.

Acknowledgments

This work was funded by the Deanship of Graduate Studies and Scientific Research at Jouf University under grant No (DGSSR-2023-02-02161).

Appendix A. Supplementary data

Supplementary data to this article can be found online at https://doi.org/10.1016/j.jsamd.2025.100965.

References

[1] K. Deshmukh, M.B. Ahamed, A.R. Polu, K.K. Sadasivuni, S.K.K. Pasha, D. Ponnamma, M.A. Al Maadeed, R.R. Deshmukh, K. Chidambaram, Impedance spectroscopy, ionic conductivity and dielectric studies of new Li^+ ion conducting polymer blend electrolytes based on biodegradable polymers for solid state battery applications, J. Mater. Sci. Mater. Electron. 27 (2016) 11410–11424, https://doi.org/10.1007/s10854-016-5267-x.

[2] B. Poyraz, A. Tozluoğlu, Z. Candan, A. Demir, M. Yavuz, Influence of PVA and silica on chemical, thermo-mechanical and electrical properties of Celluclast-treated nanofibrillated cellulose composites, Int. J. Biol. Macromol. 104 (2017) 384–392, https://doi.org/10.1016/j.ijbiomac.2017.06.018.

[3] M.B. Bechir, M. Akermi, H.J. Alathlawi, Understanding charge transport and dielectric relaxation properties in lead-free Cs_2ZrCl_6 nanoparticles, RSC Adv. 14 (2024) 14221, https://doi.org/10.1039/D4RA02031F.

[4] H.A.J. Hussien, A. Hashim, Fabrication and analysis of PVA/TiC/SiC hybrid nanostructures for nanoelectronics and optics applications, J. Inorg. Organomet. Polym. 34 (2024) 2716–2727, https://doi.org/10.1007/s10904-024-03007-5.

[5] G. Yang, Z. Yin, Q. Zha, R. Wang, Y. Xie, Y. Chen, Z. Hong, Y. Luo, M. Xue, A typha orientalis-inspired 3D Janus solar evaporator with controllable wettability for highly efficient and stable solar desalination, Desalination 595 (2025) 118318, https://doi.org/10.1016/j.desal.2024.118318.

[6] A.M. El Sayed, Synthesis, optical, thermal, electric properties and impedance spectroscopy studies on P(VC-MMA) of optimized thickness and reinforced with MWCNTs, Res. Phys. 17 (2020) 103025, https://doi.org/10.1016/j.rinp.2020.103025.

[7] T.I. Alanazi, R.A. Alenazi, A.M. El Sayed, Tuning the band gap, optical, mechanical, and electrical features of a bio-blend by Cr_2O_3/V_2O_5 nanofillers for optoelectronics and energy applications, Sci. Rep. 14 (2024) 12537, https://doi.org/10.1038/s41598-024-62643-6.

[8] W. Alharbi, K.H. Alharbi, A.S. Almuslem, M.A. El-Morsy, M.O. Farea, A. A. Menazea, Electrical conductivity and dielectric properties of tellurium (IV) oxide and copper oxide nanoparticles doped in PVA-Chitosan nanocomposite and their potential for optoelectronics devices, J. Mater. Sci. Mater. Electron. 35 (2024) 2006, https://doi.org/10.1007/s10854-024-13765-0.

[9] Y. Deng, Z. Li, Z. Yin, Y. Chen, C. Yang, Y. Luo, M. Xue, A facile method for constructing scalable and low-cost superhydrophobic coating with anti-corrosion and drag-reduction properties, Ind. Crops Prod. 216 (2024) 118732, https://doi.org/10.1016/j.indcrop.2024.118732.

[10] A.M. El Sayed, Boosting the optical and electrical properties of PVA/Na-CMC blend by Cr_2O_3 nanoparticles for photonic and energy storage applications, J. Energy Storage 82 (2024) 110609, https://doi.org/10.1016/j.est.2024.110609.

[11] C. Jin, Z. Zhang, X. Li, Silver nanoparticles stabilized by chitosan-polyvinyl alcohol polymers mediated by Pistacia extract for treatment of functional dyspepsia and gastric cancer, J. Sci. Adv. Mater. Devices 9 (2024) 100757, https://doi.org/10.1016/j.jsamd.2024.100757.

[12] I. Oreibi, M.A. Habeeb, R.S.A. Hamza, Polymer nanocomposites comprising PVA matrix and Ag–$BaTiO_3$ nanofillers: a comparative study of structural, dielectric and optical characteristics for optics and quantum nanoelectronic applications, Opt. Quant. Electron. 56 (2024) 119, https://doi.org/10.1007/s11082-023-05685-w.

[13] W.O. Obaid, A. Hashim, B.H. Rabee, Manufacturing and ameliorating the morphological, structural and optical features of PVA-CS/SiO_2-TaC futuristic Nanostructures for radiation shielding and photonics applications, J. Inorg. Organomet. Polym. Mater. (2025), https://doi.org/10.1007/s10904-025-03926-x.

[14] S.R. Al-Mhyawi, A.I. Al-Sulami, F.M.H. AlSulami, R.H. Aldahiri, M.M. Alsabban, F. M.A.B. Mosa, J.S. Alnawmasi, O. Nur, M.A. Mannaa, A. Rajeh, Synthesis, characterization, and multifunctional properties of Polyvinylpyrrolidone/Chitosan/Iron Molybdate nanocomposites for electrochemical devices, J. Sci. Adv. Mater. Devices 10 (2025) 100920, https://doi.org/10.1016/j.jsamd.2025.100920.

[15] N. Thungphotrakul, P. Prapainainar, Development of polyvinyl alcohol/carboxymethylcellulose-based bio-packaging film with citric acid crosslinking and clove essential oil encapsulated chitosan nanoparticle pickering emulsion, Int. J. Biol. Macromol. 282 (2024) 137223, https://doi.org/10.1016/j.ijbiomac.2024.137223.

[16] N. Suppanucroa, W. Yoopensuk, J. Pimoei, W. Thanapong-a-morn, W. Kao-Ian, P. Pakawanit, F. Mahlendorf, S. Kheawhom, A. Somwangthanaroj, Enhanced long-term stability of zinc-air batteries using a quaternized PVA-chitosan composite separator with thin-layered MoS_2, Electrochim. Acta 510 (2025) 145361, https://doi.org/10.1016/j.electacta.2024.145361.

[17] S. Jayaraj, P. Vellaichamy, M. Sehar, A. Ramasamy, S.K. Ponnusamy, M. O. Daramola, Enhancement in thermal, mechanical and electrical properties of novel PVA nanocomposite embedded with SrO nanofillers and the analysis of its thermal degradation behavior by nonisothermal approach, Polym. Compos. 41 (2020) 1277–1290, https://doi.org/10.1002/pc.25453.

[18] S. Panda, K. Deshmukh, S.K.K. Pasha, Dielectric, AC conductivity, and complex impedance spectroscopy studies of Ti_2CT_x MXene reinforced polyvinyl alcohol nanocomposites, Polym. Adv. Technol. 34 (9) (2023) 2974–2992, https://doi.org/10.1002/pat.6117.

[19] M. Faisal, M.M. Alam, M. Alsaiari, J. Ahmed, J.Y. Al-Humaidi, J.S. Algethami, M. A. Abdel-Fadeel, R.H. Althomali, F.A. Harraz, M.M. Rahman, J. Sci. Adv. Mater. Devices 9 (2024) 100727, https://doi.org/10.1016/j.jsamd.2024.100727.

[20] R.S.A. Hamza, M.A. Habeeb, Reinforcement of morphological, structural, optical, and antibacterial characteristics of PVA/CMC bioblend filled with SiO_2/Cr_2O_3 hybrid nanoparticles for optical nanodevices and food packing industries, Polym. Bull. 81 (2024) 4427–4448, https://doi.org/10.1007/s00289-023-04913-3.

[21] S. Alizadeh, M. Nassiri, N. Farahmandian, P. Farshi, Z.A. Ahovan, J. Majidi, A. Hashemi, S.H. Shafikhani, L. Moroni, M. Gholipourmalekabadi, Engineering of a bilayer antibacterial wound dressing from bovine pericardium and electrospun chitosan/PVA/antibiotics for infectious skin wounds management: an in vitro and

in vivo study, Int. J. Biol. Macromol. 282 (2024) 137055, https://doi.org/10.1016/j.ijbiomac.2024.137055.
[22] J. Jose, C.J. Binish, J. Johns, S.J. Chundattu, A.V. Vijayasankar, Agricultural waste valorisation – novel Areca catechu L. residue blended with PVA-Chitosan for removal of chromium (VI) from water – characterization, kinetics, and isotherm studies, Ind. Crops Prod. 222 (2024) 120013, https://doi.org/10.1016/j.indcrop.2024.120013.
[23] I.H. Ifijen, M. Maliki, I.J. Odiachi, I.C. Omoruyi, A.I. Aigbodion, E.U. Ikhuoria, Performance of metallic-based nanomaterials doped with strontium in biomedical and supercapacitor electrodes: a review, Biomed. Mater. Device. 1 (2023) 402–418, https://doi.org/10.1007/s44174-022-00006-3.
[24] A.M. Nassar, A.M. Elseman, I.H. Alsohaimi, N.F. Alotaibi, A. Khan, Diaqua oxalato strontium(II) complex as a precursor for facile fabrication of Ag-NPs@$SrCO_3$, characterization, optical properties, morphological studies and adsorption efficiency, J. Coord. Chem. 72 (5–7) (2019) 771–785, https://doi.org/10.1080/00958972.2019.1588964.
[25] Y.H. Chen, Y.C. Huang, W.D. Jiang, Study on thermal properties of nanocrystalline strontianite, J. Non-Cryst. Solids 356 (2010) 1530–1532, https://doi.org/10.1016/j.jnoncrysol.2010.04.026.
[26] L.L.Y. Chang, R.A. Howie, J. Zussman, Rock-Forming Minerals 5B: Non-silicates, 2ed, The Geological Society, London, 1998. ISBN: 9781897799901.
[27] H. Liu, M. Lin, X. Liu, Y. Zhang, Y. Luo, Y. Pang, H. Chen, D. Zhu, X. Zhong, S. Ma, Y. Zhao, Q. Yang, X. Zhang, Doping bioactive elements into a collagen scaffold based on synchronous self-assembly/mineralization for bone tissue engineering, Bioact. Mater. 5 (2020) 844–858, https://doi.org/10.1016/j.bioactmat.2020.06.005.
[28] Z. Hu, Y. Li, C. Zhang, B. Ao, Structural, electronic, optical and bonding properties of strontianite, $SrCO_3$: first-principles calculations, J. Phys. Chem. Solid. 98 (2016) 65–70, https://doi.org/10.1016/j.jpcs.2016.06.009.
[29] L. Zhang, P. Yin, J. Wang, X. Feng, J. Dai, Low-frequency microwave absorption of MOF-derived Co/CoO/$SrCO_3$@C composites, Mater. Chem. Phys. 264 (2021) 124457, https://doi.org/10.1016/j.matchemphys.2021.124457.
[30] S.A. Ehsanizadeh, A.S. Abbas, F.S. Razavi, E.A. Dawi, A.M.M. Ibrahim, M. Salavati-Niasari, Facile synthesis and characterization of $SrMnO_3$/$SrCO_3$ nanocomposites by Pechini sol-gel method as efficient and innovated active materials for electrochemical hydrogen storage application, Int. J. Hydrogen Energy 60 (2024) 392–401, https://doi.org/10.1016/j.ijhydene.2024.02.219.
[31] S.A. Ehsanizadeh, M. Goudarzi, E.A. Dawi, F.H. Alsultany, A.M. Aljeboree, M. Salavati-Niasari, Green auto-combustion synthesis of $SrNiO_3$/NiO/$SrCO_3$ ferromagnetic-nanocomposites in the presence carbohydrate sugars and their application as photocatalyst for degradation of water-soluble organic-pollutants, Alex. Eng. J. 108 (2024) 206–220, https://doi.org/10.1016/j.aej.2024.07.088.
[32] M.A. Alavi, A. Morsali, Syntheses and characterization of $Sr(OH)_2$ and $SrCO_3$ nanostructures by ultrasonic method, Ultrason. Sonochem. 17 (2010) 132–138, https://doi.org/10.1016/j.ultsonch.2009.05.004.
[33] L. Gong, T. Jiang, T. Xiao, B. Feng, M. Wei, C. Liu, W. Xiao, P. Huang, D. Huang, Biomimetic morphogenesis of strontium chitosan-gelatin composite aggregates via EPD and biomineralization in vitro and in vivo, Int. J. Nanomed. 19 (2024) 11651–11669, https://doi.org/10.2147/IJN.S476874.
[34] T.I. Alanazi, A.M. El Sayed, Structural, optical analysis, stress-strain, and dielectric properties of selenium oxide/$LaFeO_3$/blend nanocomposites with tunable properties for optoelectronics and micro-supercapacitors, J. Energy Storage 95 (2024) 112652, https://doi.org/10.1016/j.est.2024.112652.
[35] A.M. El Sayed, A.D.M. Mohamad, Synthesis, structural, thermal, optical and dielectric properties of chitosan biopolymer; influence of PVP and α-Fe_2O_3 Nanorods, J. Polym. Res. 25 (2018) 175, https://doi.org/10.1007/s10965-018-1571-x.
[36] M. Shaban, A.M. El Sayed, Effects of lanthanum and sodium on the structural, optical and hydrophilic properties of sol–gel derived ZnO films: a comparative study, Mater. Sci. Semicond. Process. 41 (2016) 323–334, https://doi.org/10.1016/j.mssp.2015.09.002.
[37] A. Hassen, A.M. El Sayed, W.M. Morsi, S. El-Sayed, Influence of Cr_2O_3 nanoparticles on the physical properties of polyvinyl alcohol, J. Appl. Phys. 112 (2012) 093525, https://doi.org/10.1063/1.4764864.
[38] G.B. Patel, N.L. Singh, F. Singh, Modification of chitosan based biodegradable polymer by irradiation with MeV ions for electrolyte applications, Mater. Sci. Eng. B 225 (2017) 150–159, https://doi.org/10.1016/j.mseb.2017.08.023.
[39] T.I. Alanazi, A.M. El Sayed, M^{3+}/$NaTiO_3$/PVA–chitosan nanocomposites (M = Ga, Ce, Nd or Er): novel solid polymer electrolytes for supercapacitors, Phys. Scripta 98 (2023) 085946, https://doi.org/10.1088/1402-4896/ace85d.
[40] J. Shi, W. Liu, X. Jiang, W. Liu, Preparation of cellulose nanocrystal from tobacco-stem and its application in ethyl cellulose film as a reinforcing agent, Cellulose 27 (2020) 1393–1406, https://doi.org/10.1007/s10570-019-02904-0.
[41] S. Saber, S. El-Sayed, A.M. El Sayed, Influence of Eu^{3+} on the structural, optical and electrical properties of PEO–PVA: dual bandgap materials for optoelectronic applications, J. Mater. Sci. Mater. Electron. 34 (2023) 406, https://doi.org/10.1007/s10854-023-09841-6.
[42] N. Algethami, Structural, optical, electrical, and DFT studies of chitosan/polyvinyl alcohol composite doped with mixed nanoparticles (GO/TiO_2) for flexible energy storage devices, J. Mater. Sci. Mater. Electron. 33 (2022) 25518–25531, https://doi.org/10.1007/s10854-022-09252-z.
[43] F.M. Ali, R.M. Kershi, Synthesis and characterization of La^{3+} ions incorporated (PVA/PVP) polymer composite films for optoelectronics devices, J. Mater. Sci. Mater. Electron. 31 (2020) 2557–2566, https://doi.org/10.1007/s10854-019-02793-w.
[44] C. Salma, B.H. Rudramadevi, Structural and photoluminescence properties of a trivalent rare earth Sm ion-doped PVA/PVP blend polymer films, Ferroelectrics Lett. 49 (1–3) (2022) 30–44, https://doi.org/10.1080/07315171.2022.2076464.
[45] G. Mohammed, A.M. El Sayed, Structural, morphological, optical and dielectric properties of M^{3+}/PVA/PEG SPE Films (M = La, Y, Fe or Ir), Polym. Adv. Technol. 30 (2019) 698–712, https://doi.org/10.1002/pat.4508.
[46] M. Radaoui, A.B. Fredj, S. Romdhane, N. Bouguerra, D.A.M. Egbe, H. Bouchriha, New conjugated polymer/fullerene nanocomposite for energy storage and organic solar cell devices: studies of the impedance spectroscopy and dielectric properties, Synth. Met. 283 (2022) 116987, https://doi.org/10.1016/j.synthmet.2021.116987.
[47] R. Chakroun, B. Jamoussi, B. Al-Mur, A. Timoumi, K. Essalah, Impedance spectroscopy and dielectric relaxation of ImidazoleSubstituted palladium(II) phthalocyanine (ImPdPc) for organic solar cells, ACS Omega 6 (16) (2021) 10655–10667, https://doi.org/10.1021/acsomega.1c00034.
[48] R. Jacob, H.G. Nair, J. Isac, Impedance spectroscopy and dielectric studies of nanocrystalline iron doped barium strontium titanate ceramics, Process. Appl. Ceram. 9 (2) (2015) 73–79, https://doi.org/10.2298/PAC1502073J.
[49] M.L. Verma, H.D. Sahu, Study on ionic conductivity and dielectric properties of PEO-based solid nanocomposite polymer electrolytes, Ionics 23 (2017) 2339–2350, https://doi.org/10.1007/s11581-017-2063-4.
[50] E.M. Abdelrazek, A.M. Abdelghany, A.E. Tarabiah, H.M. Zidan, AC conductivity and dielectric characteristics of PVA/PVP nanocomposite filled with MWCNTs, J. Mater. Sci. Mater. Electron. 30 (2019) 15521–15533, https://doi.org/10.1007/s10854-019-01929-2.